Ultra-sharp pinnacles sculpted by natural convective dissolution

Jinzi Mac Huang[a], **Joshua Tong**[a], **Michael Shelley**[a,b,1], **and Leif Ristroph**[a,1]

[a]Applied Math Lab, Courant Institute, New York University, New York, NY 10012; and [b]Center for Computational Biology, Flatiron Institute, New York, NY 10010

Edited by David A. Weitz, Harvard University, Cambridge, MA, and approved July 2, 2020 (received for review January 26, 2020)

The evolution of landscapes, landforms, and other natural structures involves highly interactive physical and chemical processes that often lead to intriguing shapes and recurring motifs. Particularly intricate and fine-scale features characterize the so-called karst morphologies formed by mineral dissolution into water. An archetypal form is the tall, slender, and sharply tipped karst pinnacle or rock spire that appears in multitudes in striking landforms called stone forests, but whose formative mechanisms remain unclear due to complex, fluctuating, and incompletely understood developmental conditions. Here, we demonstrate that exceedingly sharp spires also form under the far-simpler conditions of a solid dissolving into a surrounding liquid. Laboratory experiments on solidified sugars in water show that needlelike pinnacles, as well as bed-of-nails-like arrays of pinnacles, emerge robustly from the dissolution of solids with smooth initial shapes. Although the liquid is initially quiescent and no external flow is imposed, persistent flows are generated along the solid boundary as dense, solute-laden fluid descends under gravity. We use these observations to motivate a mathematical model that links such boundary-layer flows to the shape evolution of the solid. Dissolution induces these natural convective flows that, in turn, enhance dissolution rates, and simulations show that this feedback drives the shape toward a finite-time singularity or blow-up of apex curvature that is cut off once the pinnacle tip reaches microscales. This autogenic mechanism produces ultra-fine structures as an attracting state or natural consequence of the coupled processes at work in the closed solid-fluid system.

geomorphology | fluid–structure interaction | dissolution | natural convection | stone forest

The tall and pointed rock spires, or pinnacles, of Fig. 1 stand in sharp contrast to the smoothed shapes and shallow slopes commonly associated with erosion and weathering. That pinnacles appear in multitudes in vast arrays called stone forests (1, 2), and that such landforms are found worldwide (3–7) suggests robust mechanisms underlying their development. These structures are examples of karst topographies that form by mineral dissolution in water (2, 8), but the environmental and hydrological conditions essential to their formation are unclear. Geomorphological studies have detailed the rich developmental histories of stone forests involving, among many other complexities, periods of complete or partial submersion under water, burial under loose sediment, and exposure to surface erosion (3–7, 9). While superficial features such as channels and grooves seem linked to rain runoff (2), it is unclear how much shape development occurred prior to surface processes. Further, stone forests have been discovered buried under loose sediment (10), suggesting that surface erosion is not essential to the pinnacle motif. Mineral spires can result from complete submersion under water followed by drainage (11), though the degree of shape development during these stages is unclear. Given the uncertainties regarding which factors are most critical, the study of pinnacle formation may benefit from laboratory experiments in which conditions can be imposed and cleanly controlled and the relevant shape developments observed and measured.

Viewed mathematically and physically, the action of erosion, dissolution, or melting on stone, soil, sand, ice, and other natural materials can be categorized as free- or moving-boundary problems (12, 13). This perspective is especially useful for understanding fundamental shape-changing mechanisms and for disentangling the interdependent solid and fluid dynamics that arise when boundaries are carved by flowing air or water (14–16). The study of shape–flow interactions also benefits from laboratory experiments, which complement geomorphological field studies by permitting observation and measurement on tractable length and time scales and under controlled and reproducible conditions (17). Experiment and mechanistic theory, including mathematical modeling and simulation, have been usefully applied toward problems ranging from the growth and form of icicles (18) to landforms such as dunes (19), large-scale landscapes (20–22), and even global-scale flow–structure couplings such as continental drift driven by mantle convection (23, 24).

These past successes motivate the application of the moving-boundary approach to dissolution and toward understanding karst morphologies and pinnacles specifically. Here, we show experimentally and theoretically that ultra-sharp pinnacles emerge robustly as natural consequences of dissolution in the presence of gravity. Building on recent work (25–27), we conduct clean and controlled laboratory experiments aimed at understanding the minimal conditions needed to form pinnacles. Precision measurements allow for close comparison with a moving-boundary mathematical model that incorporates the relevant flow physics and chemistry of dissolution. Together, these

Significance

This work reveals a mechanism that may contribute to the formation of sharply pointed rock spires in karst or dissolved landforms such as stone forests. We show that solids dissolving into liquids in the presence of gravity naturally produce flows that carve ultra-sharp spikes. Better understanding the origin of these delicate structures may aid in natural conservation efforts. Our experimental and theoretical techniques may also be applied to other problems in geomorphology and phase-change processes such as ice melting. The mechanism could be used to manufacture fine-scale structures, and our theory provides the relevant control parameters.

Author contributions: J.M.H., M.S., and L.R. designed research; J.M.H., J.T., M.S., and L.R. performed research; J.M.H., J.T., M.S., and L.R. analyzed data; and J.M.H., M.S., and L.R. wrote the paper.

The authors declare no competing interest.

This article is a PNAS Direct Submission.

[1] To whom correspondence may be addressed. Email: ristroph@cims.nyu.edu or shelley@cims.nyu.edu.

This article contains supporting information online at https://www.pnas.org/lookup/suppl/doi:10.1073/pnas.2001524117/-/DCSupplemental.

Fig. 1. Natural pinnacles and stone forests. (*A*–*C*) Photographs showing limestone structures of different scales in the Tsingy de Bemaraha National Park in Madagascar. *A*–*C*: Image credit: Stephen Alvarez (photographer). (*D*) Similar limestone formations in the Gunung Mulu National Park of Malaysia. *D*: Image credit: Grant Dixon (photographer).

methods uncover a self-sculpting process by which the flows naturally generated during dissolution also reshape solids into microscopically sharp spikes. Because it is at work under commonplace conditions, we speculate that this mechanism contributes to the formation of pinnacles in nature.

Results

Laboratory Experiments. To assess experimentally the development of a dissolving solid under idealized and controlled conditions, we consider objects made of solidified sugars cast into simple initial shapes and submerged into a large tank of water (Fig. 2*A*). The relatively high solubility of sugars in comparison to natural minerals allows for tractable run times of hours. The initial form resembles an upright cylinder supported from below, and its apex is smooth and blunt. This starting shape can be viewed as analogous to the vertical columns formed between intersecting planar fissures that are thought to initiate pinnacle karst (3–7, 9). The choice of a tall column extends the dissolution process and allows for observation of the long-time shape dynamics. The object, which is observed to retain axisymmetry, is photographed over time by two cameras, one of which is fixed and captures the entire boundary and the other mounted to a moving stage to follow the apex and capture zoomed-in images. Additional experimental details are available in *Materials and Methods* and *SI Appendix*.

The overlaid images of Fig. 2*B* and the corresponding Movie S1 show a typical trial. The initially rounded column is seen to sharpen into a needle-like spire as the boundaries recede. Boundary profiles extracted from photographs are shown in Fig. 2 *C* and *E*, the latter in the frame of the descending tip. Strikingly, these data indicate that the object becomes ever more slender and its tip ever sharper throughout the dissolution process. These observations are reproducible across trials and for different initial geometries, as supported by the extended data figures in *SI Appendix*.

A critical, but unseen, factor in these shape dynamics is the role of flow. Although the water is initially quiescent, and no external flow is imposed throughout our experiments, the fluid is brought into motion by the dissolution process itself. To visualize these flows, we perform separate experiments in which we seed the water with microparticles and illuminate from above with planar laser light. As shown in Fig. 2 *G* and *H*, time-exposed photographs capture pathlines indicative of flows of speeds on the order of 1 cm/s that descend along the surface. This effect can be attributed to the fact that the solid is denser than the liquid and that flows are generated along the surface as the dense, solute-laden fluid descends under gravity.

A Moving-Interface Model. Close inspection of the experimental shapes of Fig. 2 *B* and *C* reveals that the pinnacle tip experiences higher dissolution rate than other locations on the surface, and yet the apex is not blunted, but, rather, sharpens. Such

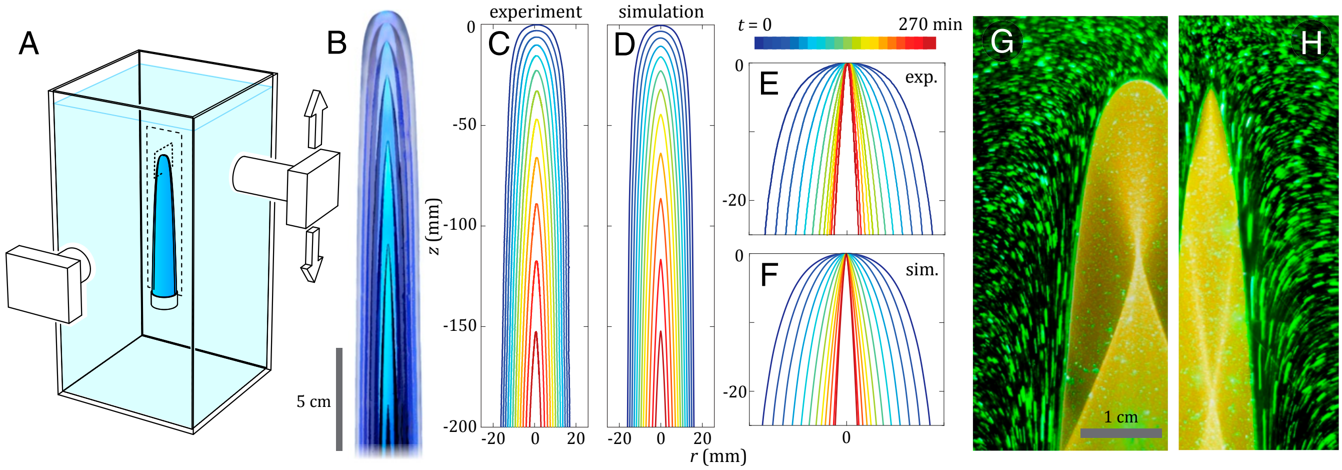

Fig. 2. Emergence of pinnacles in experiment and simulation. (*A*) Laboratory experiments. An upright object cast from solidified sugars dissolves in a large tank of water. One camera captures full-view images of the solid as it develops in time, and a second is zoomed in and follows the apex region. (*B*) Overlaid full-view images spaced at an interval of 50 min. (*C*) Solid–liquid boundary profile extracted from full-view images and displayed every 25 min. (*D*) Corresponding boundary profiles as computed by the simulation. (*E* and *F*) Development of the apex region in experiment (exp.) and simulation (sim.). These profiles are shown in the moving frame of the apex, revealing a trend toward sharper structures. (*G* and *H*) Flow visualization via pathline photography of microparticles illuminated by a laser sheet. Flows descend along the surface and entrain fluid from the sides at both early and later times.

paradoxes are best resolved by mathematical treatment as a free- or moving-boundary problem (12), in which the solid–liquid interface is viewed as a receding surface whose dynamics are dictated by the physics, chemistry, and fluid dynamics of dissolving (28, 29). The natural convective flows observed in experiments are expected to play the important role of transporting solute along the surface. These flows thus modify the local solute concentration and the local dissolution rate, which Fick's law of diffusion dictates as proportional to the gradient in solute concentration normal to the surface (28). These effects are incorporated into a mathematical model by using boundary-layer theory (29), which describes the flow and concentration fields that vary strongly within a thin region of the fluid surrounding the solid. In this way, we arrive at an evolution equation for the interface in which the local normal velocity is related to the global shape. The dissolution rate is also subject to the Gibbs–Thomson effect, which acts to enhance dissolution rates in proportion to local curvature (30, 31). Complete model derivations, as well as details of their numerical solution, are given in *Materials and Methods* and *SI Appendix*.

Our model furnishes boundary dynamics in remarkable agreement with experiments, as shown in Fig. 2 *D* and *F* and Movie S2. Notably, we recover the observed tendency toward a sharp pinnacle, and this behavior is robust to initial shape and to model parameters (*SI Appendix*). Taken together, these results indicate that pinnacles emerge as the shape attractors for solids dissolving into fluids in the presence of gravity.

Pinnacle Formation as a Geometric Shock and Curvature Singularity. Further analysis of the shape dynamics in experiment and theory reveals a common approach to the formation of a sharp apex. The boundary shape can be represented by revolving a planar curve γ that is characterized by its tangent angle $\theta(s,t)$ as a function of arclength s and time t, as defined in Fig. 3*A*. As shown in the plot of Fig. 3*C*, curves of $\theta(s,t)$ over time for the simulations of Fig. 2 show an approach to an abrupt drop in the tangent angle, which is suggestive of a geometric shock (32). As shown in Fig. 3*B*, another signature of a shock can be seen in the converging characteristic curves that represent trajectories of points propagated normally to the boundary (32). Further, local curvature is given by $\kappa(s,t) = -\partial\theta/\partial s$ and plotted in Fig. 3*D*, where unbounded growth of curvature quantifies the sharpening dynamics.

These observations are further elucidated by an analysis of our model equations showing that, if only hydrodynamic (boundary-layer flows), but not thermodynamic (Gibbs–Thomson), effects are included, then the pinnacle evolves to infinite apex curvature $\kappa_0(t) = \kappa(s=0,t)$ in finite time. We derive a power law for this mathematical singularity as $\kappa_0(t) = \kappa_0(0)(1-t/t_s)^{-4/5}$, where $\kappa_0(0)$ is the initial tip curvature and $t_s > 0$ is the time at which the singularity develops (*SI Appendix*). This analysis motivates a recasting of the curvature dynamics as $\bar{\kappa}_0(t)^{-5/4} = [\kappa_0(t)/\kappa_0(0)]^{-5/4}$, and, indeed, the experimental and model data of Fig. 3*F* follow the expected linear trend until late times.

In the later stages of dissolution, Fig. 3*F* shows that the curvature growth continues, but at a nonsingular pace. This may be attributed to the Gibbs–Thomson effect, which strongly enhances the dissolution rate at the apex, blunting the tip and cutting off the singularity. In experiments, the radius of curvature of the tip eventually reaches tens of micrometers and approaches the imaging resolution of our system (*Materials and Methods* and *SI Appendix*). Theory predicts an ultimate fineness on the order of 10 µm, a value set by material parameters.

Pinnacle Forests from Dissolution of Porous Solids. Returning to the motivating landforms of Fig. 1, we next ask how dissolution and the dissolutive sharpening mechanism described above might produce many spires in parallel. We hypothesize that the fluid-filled pores or fissures in a porous, soluble material serve as conduits for the flows produced during dissolution. Initially small, such cavities expand as their walls are consumed by the dissolving action and eventually merge or collide into one another. The interstitial solid regions may be shaped into pillars by the downward convective flows and then sharpened into pinnacles by the mechanism studied here. We experimentally test this picture in a highly idealized scenario of a soluble, solid block seeded with an array of pores and immersed in liquid. Casting molten sugars in a mold containing thin wires, which are removed after solidification, yields a large block spanned by vertical pores that are arranged in a square lattice (*Materials and Methods*). The block is supported on an elevated base

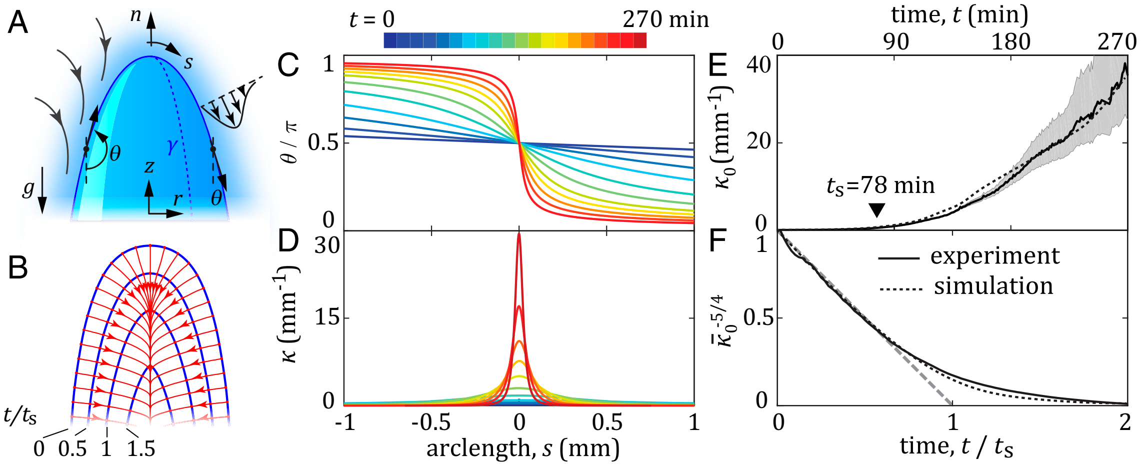

Fig. 3. Pinnacle formation as a geometric shock or curvature singularity. (*A*) Schematic defining the model and its variables. A solid of axisymmetric shape dissolves into surrounding liquid and boundary-layer flows are induced as dense, solute-laden fluid descends under gravity. (*B*) Shape evolution near the apex from simulation. The singularity or shock-formation time t_s is associated with the intersection of characteristic curves (red). (*C*) Shape development as quantified by tangent angle θ versus arclength *s*. The approach to a step function is a signature of a geometric shock. (*D*) Shape development as quantified by curvature κ. The blow-up of the apex curvature is a signature of a mathematical singularity. (*E*) Unbounded growth of apex curvature in experiment and simulation. The gray region represents error bars propagated based on the experimental resolution. (*F*) Power-law behavior of curvature in the lead-up to the shock or singularity.

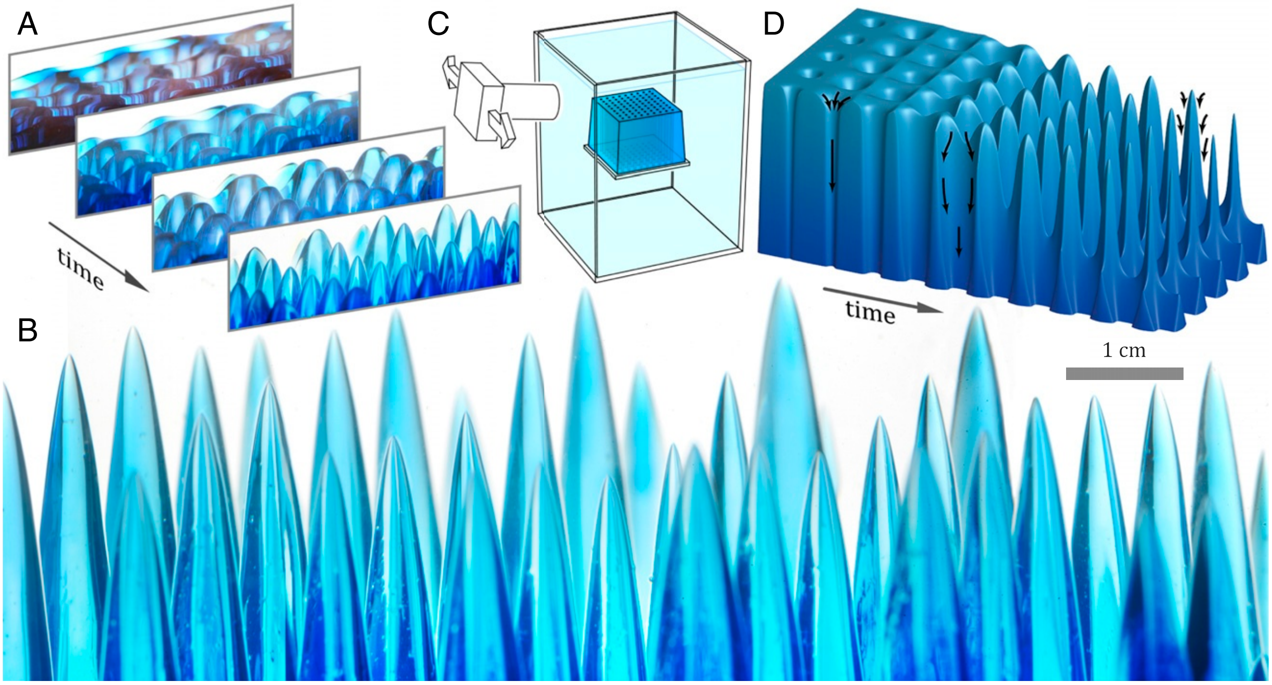

Fig. 4. Bed-of-nails morphology from dissolution of a porous solid. (*A*) Temporal progression of a dissolving block seeded with vertical pores. The openings widen and in their interstices develop into rounded hills, which then steepen into pillars. (*B*) The pillars sharpen to form an array of pinnacles. (*C*) Experimental schematic. A block of solidified sugar is cast with vertical pores and then immersed in water and imaged. (*D*) Interpretive schematic showing shape progression and expected flow structure.

and entirely submerged under water, where it is photographed over time (Fig. 4*C*). The pores run the height of the block and base, allowing fluid to be conveyed downward during the dissolution process.

As shown in the photographs of Fig. 4 *A* and *B* and Movie S3, the solid undergoes dramatic changes in shape as it dissolves. At early times, the openings of the pores on the upper surface widen, and the pores thus take on a fluted sectional profile, as shown schematically in Fig. 4*D*. This may be attributed to higher dissolution rates near the openings as fresh water from above is drawn downward by natural convective flows. As they widen further, each set of four neighboring pores in the square lattice begins to collide or merge near their tops, yielding soft hilltops in their interstices and, thus, a gently rolling landscape dotted with sinkholes. The hillslopes then steepen to form distinct pillars, whose rounded tops later sharpen into spires. In this final stage, each pinnacle in the array may be thought to develop independently and by the mechanism studied here, as the flows responsible for sculpting are confined to thin boundary layers. These events yield a bed-of-nails morphology, here, a square lattice of spikes that reflects the initial lattice of pores. More random seeding of pore locations is expected to generate disordered arrays of pinnacles of varying girth and height, which may more closely resemble natural pinnacles and stone forests.

Discussion and Conclusions

The tendency toward sharp structures can be understood qualitatively by noting that the entrainment into the surface flows of fresh fluid from the sides (Fig. 2 *G* and *H*) tends to thin the concentration boundary layer and, thus, enhance dissolution rates. This mechanism of dissolutive sharpening requires only the commonplace conditions of a solid dissolving into liquid and the consequent density variations and natural convective flows. It relies on stably attached boundary layers, which can be expected of the upper surface of a solid if the solute-laden fluid is denser than the far-field fluid (29). Gravitationally stable boundary layers in an inverted situation can be expected for lower surfaces and low-density, upwardly buoyant flows, as is expected for the underside of an iceberg melting in cold waters (17). More generally, one anticipates parallels between melting and dissolution, with temperature playing a role analogous to solute concentration (29). For both processes, our model framework is general and versatile enough to address further questions of shape dynamics.

The conditions studied here are purposefully idealized, permitting clear identification and clean characterization of dissolutive sharpening, its chemophysical mechanism, and mathematical structure. By showing that pinnacle-like shapes arise spontaneously in closed solid–fluid systems, under constant conditions, and without external forcing beyond that of gravity, this study reveals a minimal set of ingredients essential to the needle and bed-of-nails motifs. Our experimental pinnacles are carved by boundary-layer flows generated by the dissolution process itself, whereas in nature, the responsible flows may include subsurface drainage and surface runoff (2, 4, 9, 11). Our pinnacle arrays form via dissolutive widening of pores, whose initial arrangement set the pattern of pinnacles, and a similar progression toward stone forests is thought to be initiated by vertical columns between intersecting fissures (3–7, 9). Ultimately, similar shapes are observed in both the synthetic and natural systems, the former being associated with an attractor of the shape dynamics that emerges as details of the initial form are lost in the approach to a singularity.

Future work might assess the robustness of pinnacle formation for differing environmental conditions through laboratory experiments, models, and simulations of the type presented here. For example, the effect of precipitation and surface runoff could be isolated for study by subjecting a soluble body in air to misting with water droplets or some other form of simulated rain (2). Corresponding theory should account for dissolution into thin-film flows. Pinnacle formation while buried under loose sediment could be tested by using sand or other granular material saturated with water (11), a model or simulation of which should account for the Darcy flow conditions in the porous medium. In such scenarios, the hydrological conditions may be held constant as in our study, or be subject to time variations, say, by cyclic draining and immersion. Results from all such studies would help to tell the origin story of these striking landforms, whose ultra-fine features require special conservation efforts (33–35).

Materials and Methods

Materials and Fabrication. Objects made of solidified sugars are manufactured by combining granulated table sugar, corn syrup, and water in proportion $8:3:2$ by volume. The mixture is stirred continuously and brought to 150°C, at which point it is abruptly taken off the heat. The molten sugars are immediately poured into custom-shaped molds and allowed to gradually set over 12 h or longer, which permits bubbles to rise out. This recipe achieves so-called hard-crack candy, which is an amorphous solid of about 99% sugar content. Cylindrical molds of about 25-cm height and diameters between 2 and 6 cm are used to make the pillars in the single-pinnacle experiments. Once removed from the mold, the solid cylinder is reshaped on a spinning stage by dissolving with warm water applied with a sponge. This gives an initial form that is axisymmetric with a rounded top and slightly tapered sides. A cubic mold measuring $10 \times 10 \times 10$ cm in length, width, and height is used for the pinnacle-array experiments. The bottom of the mold receives metal rods of diameter 0.4 cm that stand upright in a square 7-by-7 array of spacing 1.3 cm. After casting, the rods are removed to leave an array of pores that vertically span the block.

Dissolution Experiments and Image Acquisition. The experiments are conducted in a clear acrylic (plexiglass) tank measuring $30 \times 30 \times 60$ cm in length, width, and height that is filled with degassed water at room temperature of 23 ± 1°C. The depth of the tank allows the dense fluid containing dissolved sugars to settle at the bottom and far from the test object. Image acquisition is accomplished by two synchronized Nikon D610 digital cameras capturing photographs at 1-min intervals and directed normally to two adjacent side walls. Each is backlit with cold light-emitting diode (LED) lights shone on a diffusive screen. On the screen and on either side of the object are opaque sheets, whose refraction through the object cause the boundary to appear dark on the light background. The zoomed-out camera is fixed in position and captures the overall shape of the dissolving object with resolution 11.3 pixels/mm. The zoomed-in camera is fitted with a macro lens and captures images around the apex at resolution 173 pixels/mm. For the single-pinnacle experiments, this camera is mounted on a vertical translation stage so that the apex may be maintained in the center of view throughout the experiment. For the pinnacle-array experiments, the zoomed-in camera is mounted on a horizontal stage and panned across the upper surface as several photographs are taken. These images are later digitally registered and combined.

Image Processing and Profile Extraction. For the single pinnacles, the contour of the interface is extracted via a custom-written MATLAB code using the Image Processing Toolbox. For the zoomed-in images, the contour near the apex is fit to a fourth-order polynomial, and the spatial distribution of the tangent angle $\theta(s,t)$ and the apex curvature $\kappa_0(t)$ are then computed from the fit.

Boundary–Layer Theory Model and Shock Formation. The solid–liquid interface recedes with velocity proportional to the normal gradient of concentration, $V_n \sim \mathbf{n} \cdot \nabla c$, where the prefactor may be calculated from conservation of mass and Fick's law of diffusion. The concentration field c and its gradient at the interface are obtained from boundary-layer theory, yielding the expression $V_n(s,t) = -a[r(s,t)\cos\theta(s,t)]^{1/3} / [\int_0^s r(s',t)^{4/3} \cos^{1/3}\theta(s',t) ds']^{1/4}$ for the local dissolution rate as a function of the shape, expressed here as the tangent angle $\theta(s,t)$ at each location s and time t. Here, the constant $a \sim 10^{-7}$ m$^{5/4}$/s is estimated from material properties in experiment. The axisymmetric geometry of the dissolving object is characterized by revolving a planar curve γ around the z axis, as shown in Fig. 3*A*. The evolution of γ is then prescribed by $\partial_t\theta - V_s\partial_s\theta = \partial_s V_n$. The prescription of a tangential velocity V_s does not change the shape, but is imposed in order to preserve the spacing in arclength so that s and t remain independent variables. The s-derivative of the θ equation in the limit as $s \to 0$ leads to an ordinary differential equation for the apex curvature, $d\kappa_0/dt = -\partial_s^2 V_n(0,t) - V_n(0,t)\kappa_0^2 \sim \kappa_0^{9/4}$, whose solution diverges in finite time.

Gibbs–Thomson Effect. The Gibbs–Thomson effect describes the effect of curvature on the saturation concentration at a solid–liquid interface: $c_s^* = c_s \exp(\epsilon\hat{\kappa})$ for a surface of mean curvature $\hat{\kappa}$, where c_s is associated with a flat interface ($\hat{\kappa} = 0$). Here, $\epsilon \approx 10$ μm is a material parameter estimated for our experimental conditions. As compared to a flat interface of dissolution rate V_n, a curved surface has enhanced saturated concentration and, thus, enhanced dissolution rate of the form $V_n^* = V_n(1 + \epsilon\hat{\kappa})$. In the θ dynamical equation, this effect manifests as a diffusion term that suppresses high curvature by enhancing dissolution rate. At the apex, the two principal curvatures are identical and, thus, $\hat{\kappa}(0,t) = \kappa_0(t)$, and the Gibbs–Thomson effect becomes significant when $1/\kappa_0 \approx \epsilon \approx 10$ μm.

Simulation Method and Implementation. A custom-written numerical scheme employs the $\theta - L$ method to solve dynamical equations for the tangent angle θ and total arclength L (36). The numerical simulations are performed in MATLAB with second-order finite differences in space. In time, a second-order Adam–Bashforth backward differentiation method mitigates the stiffness and nonlinearity of the equations. Consistent parameter values of $a = 4.5 \times 10^{-7}$ m$^{5/4}$/s and $\epsilon = 11$ μm are used throughout all examples in this article and the figures in *SI Appendix*. These values are set by matching the evolution of tip curvature κ_0 and the total arclength L for the experiment in Figs. 2 and 3, and the resulting choice leads to excellent agreement across all experiments.

Data Availability. Measured shape profiles over time for all four single-pinnacle experiments, as well as corresponding simulation results, are available in *SI Appendix*. Raw images, movies, data files, and analysis codes will be provided upon request to the authors.

ACKNOWLEDGMENTS. We thank M. Davies Wykes, S. Childress, and J. Zhang for useful discussions. We acknowledge support from the NSF through the grant CBET-1805506 and from the Lilian and George Lyttle Chair of Applied Mathematics.

1. M. M. Sweeting, *Karst in China: Its Geomorphology and Environment* (Springer Verlag, Berlin, Germany, 1995).
2. A. Ginés, M. Knez, T. Slabe, W. Dreybrodt, *Karst Rock Features: Karren Sculpturing* (Založba ZRC, Ljulbljana, Slovenia, 2009).
3. R. Ley, The pinnacles of Gunung Api. *Geogr. J.* **146**, 14–21 (1980).
4. L. H. Song, Origination of stone forests in China. *Int. J. Speleol.* **15**, 3–13 (1986).
5. M. Veress, D. Lóczy, Z. Zentai, G. Tóth, R. Schläffer, The origin of the Bemaraha tsingy (Madagascar). *Int. J. Speleol.* **37**, 131–142 (2008).
6. M. Veress, G. Toth, Z. Zentai, R. Schläffer, The Ankarana tsingy and its development. *Carpathian J. Earth Environ. Sci.* **4**, 95–108 (2009).
7. M. Veress, Z. Zentai, K. Péntek, L. Döbröntei, L. D. Kiprijanova, The development of the pinnacles (Lena pillars) along Middle Lena (Sakha Republic, Siberia, Russia). *Proc. Geol. Assoc.* **125**, 452–462 (2014).
8. D. Ford, P. D. Williams, *Karst Hydrogeology and Geomorphology* (John Wiley & Sons, West Sussex, England, 2013).
9. P. Jian *et al.*, Relating aerial erosion, soil erosion and sub-soil erosion to the evolution of Lunan Stone Forest, China. *Earth Surf. Process. Landforms* **32**, 260–268 (2007).
10. M. Knez, B. Otoničar, T. Slabe, Subcutaneous stone forest (Trebnje, central Slovenia). *Acta Carsol.* **32**, 29–38 (2003).
11. T. Slabe, A. Hada, M. Knez, Laboratory modeling of karst phenomena and their rock relief on plaster: Subsoil karren, rain flutes karren and caves. *Acta Carsol.* **45**, 187–204 (2016).
12. J. Crank, *Free and Moving Boundary Problems* (Clarendon Press, Oxford, UK, 1984).
13. L. Ristroph, Sculpting with flow. *J. Fluid Mech.* **838**, 1–4 (2018).
14. L. Ristroph, M. N. Moore, S. Childress, M. J. Shelley, J. Zhang, Sculpting of an erodible body by flowing water. *Proc. Natl. Acad. Sci. U.S.A.* **109**, 19606–19609 (2012).
15. M. N. Moore, L. Ristroph, S. Childress, J. Zhang, M. J. Shelley, Self-similar evolution of a body eroding in a fluid flow. *Phys. Fluids* **25**, 116602 (2013).
16. K. Amin, J. Mac Huang, K. J. Hu, J. Zhang, L. Ristroph, The role of shape-dependent flight stability in the origin of oriented meteorites. *Proc. Natl. Acad. Sci. U.S.A.* **116**, 16180–16185 (2019).
17. H. E. Huppert, The physical processes involved in the melting of icebergs. *Ann. Glaciol.* **1**, 97–101 (1980).
18. M. B. Short, J. C. Baygents, R. E. Goldstein, A free-boundary theory for the shape of the ideal dripping icicle. *Phys. Fluids* **18**, 083101 (2006).
19. P. Hersen, S. Douady, B. Andreotti, Relevant length scale of barchan dunes. *Phys. Rev. Lett.* **89**, 264301 (2002).

20. H. H. Stølum, River meandering as a self-organization process. *Science* **271**, 1710–1713 (1996).
21. J. T. Perron, J. W. Kirchner, W. E. Dietrich, Formation of evenly spaced ridges and valleys. *Nature* **460**, 502–505 (2009).
22. SD. Willett, S. W. McCoy, J. T. Perron, L. Goren, C. Y. Chen, Dynamic reorganization of river basins. *Science* **343**, 1248765 (2014).
23. M. Gurnis, Large-scale mantle convection and the aggregation and dispersal of supercontinents. *Nature* **332**, 695–699 (1988).
24. J. Zhang, A. Libchaber, Periodic boundary motion in thermal turbulence. *Phys. Rev. Lett.* **84**, 4361–4364 (2000).
25. E. Nakouzi, R. E. Goldstein, O. Steinbock, Do dissolving objects converge to a universal shape?. *Langmuir* **31**, 4145–4150 (2014).
26. J. Mac Huang, M. N. J. Moore, L. Ristroph, Shape dynamics and scaling laws for a body dissolving in fluid flow. *J. Fluid Mech.* **765**, R3 (2015).
27. M. S. D. Wykes, J. Mac Huang, G. A. Hajjar, L. Ristroph, Self-sculpting of a dissolvable body due to gravitational convection. *Phys. Rev. Fluids* **3**, 043801 (2018).
28. V. G. Levich, *Physicochemical Hydrodynamics* (Prentice-Hall Inc., Upper Saddle River, NJ, 1962).
29. H. Schlichting, K. Gersten, *Boundary-Layer Theory* (Springer, Berlin, Germany, 2016).
30. H. Aaron, G. Kotler, The effects of curvature on the dissolution kinetics of spherical precipitates. *Metal Sci. J.* **4**, 222–225 (1970).
31. M. Perez, Gibbs–Thomson effects in phase transformations. *Scripta Mater.* **52**, 709–712 (2005).
32. L. Evans, *Partial Differential Equations* (Graduate Studies in Mathematics, American Mathematical Society, Providence, RI, 2010), vol. 19.
33. E. Hamilton-Smith, Karst and world heritage status. *Acta Carsol.* **36**, 291–302 (2007).
34. T. Raharimahefa, Geoconservation and geodiversity for sustainable development in Madagascar. *Madagascar Conserv. Develop.* **7**, 126–134 (2012).
35. C. Zhang, M. Day, W. Li, Landuse and land cover change in the Lunan Stone Forest, China. *Acta Carsol.* **32**, 161–174 (2016).
36. T. Y. Hou, J. S. Lowengrub, M. J. Shelley, Removing the stiffness from interfacial flows with surface tension. *J. Comput. Phys.* **114**, 312–338 (1994).